# Lab on a Chip

## Motile cells as probes for characterizing acoustofluidic devices

| | |
|---|---|
| Journal: | *Lab on a Chip* |
| Manuscript ID | LC-ART-10-2020-001025.R1 |
| Article Type: | Paper |
| Date Submitted by the Author: | 23-Dec-2020 |
| Complete List of Authors: | Kim, Minji; Washington University in St Louis McKelvey School of Engineering, Mechanical Engineering & Materials Science<br>Bayly, Philip; Washington University in St Louis McKelvey School of Engineering, Mechanical Engineering & Materials Science<br>Meacham, J.; Washington University in St Louis McKelvey School of Engineering, Mechanical Engineering and Materials Science |
| | |

## SCHOLARONE™
## Manuscripts

# Motile cells as probes for characterizing acoustofluidic devices

Minji Kim,[a] Philip V. Bayly,[a] and J. Mark Meacham*[a]

Acoustic microfluidics has emerged as a versatile solution for particle manipulation in medicine and biology. However, current technologies are largely confined to specialized research laboratories. The translation of acoustofluidics from research to clinical and industrial settings requires improved consistency and repeatability across different platforms. Performance comparisons will require straightforward experimental assessment tools that are not yet available. We introduce a method for characterizing acoustofluidic devices in real-time by exploiting the capacity of swimming micro-organisms to respond to changes in their environment. The unicellular alga, *Chlamydomonas reinhardtii*, is used as an active probe to visualize the evolving acoustic pressure field within microfluidic channels and chambers. In contrast to more familiar mammalian cells, *C. reinhardtii* are simple to prepare and maintain, and exhibit a relatively uniform size distribution that more closely resembles calibration particles; however, unlike passive particles, these motile cells naturally fill complex chamber geometries and redistribute when the acoustic field changes or is turned off. In this way, *C. reinhardtii* cells offer greater flexibility than conventional polymer or glass calibration beads for *in situ* determination of device operating characteristics. To illustrate the technique, the varying spatial density and distribution of swimming cells are correlated to the acoustic potential to automatically locate device resonances within a specified frequency range. Peaks in the correlation coefficient of successive images not only identify the resonant frequencies for various geometries, but the peak shape can be related to the relative strength of the resonances. Qualitative mapping of the acoustic field strength with increasing voltage amplitude is also shown. Thus, we demonstrate that dynamically responsive *C. reinhardtii* enable real-time measurement and continuous monitoring of acoustofluidic device performance.

## Introduction

Acoustofluidics is promoted as an enabling technology in medicine and biology, among other fields that involve controlled motion of fluids and particles (e.g., nanomaterial synthesis,[1-4] rapid prototyping/3D printing,[5-7] and transport process management[8-10]). Integration of acoustic waves permits non-contact object manipulation and analysis in microfluidic formats. Further, the safety and biocompatibility of ultrasound exposure are well-established.[11-15] The versatility of the method has driven its rapid adoption in many areas of biomedical research. Size-selective sorting, isolation, and trapping have been demonstrated for objects sized from tens of nanometers (biomolecules) to tens of microns (cells/microorganisms) subject to the target particles having a sufficiently unique acoustophysical signature—mass density, compressibility, and size. To date, acoustic microfluidic devices have been applied to isolation of extracellular vesicles and lipoproteins,[16-18] separation/detection of bacteria,[19, 20] enrichment of circulating tumor cells,[21, 22] assembly of cell aggregates for drug screening and tissue engineering applications,[23, 24] trapping of swimming algae cells,[25] and rotational manipulation of larger micro-organisms.[26]

Computational modeling and laboratory-scale prototypes promise substantial advantages for acoustofluidic mixing, particle sorting, isolation, and analysis; however, despite this tremendous potential, inconsistency and poor reproducibility hinder translation of acoustofluidic technologies to clinical practice and industrial use. Precise and stable operation remains a significant challenge due to the sensitivity of performance on system geometric tolerances and difficult-to-control environmental variables (e.g., temperature). Rapid and accurate experimental characterization methods are needed to improve robustness and to facilitate eventual standardization. Such approaches would accelerate the design process, while also allowing real-time identification of system operating parameters and feedback control.

Significant effort has focused on model-based acoustic microfluidic design and optimization to minimize losses and maximize the figure of merit for device effectiveness (e.g., acoustic pressure or pressure gradient).[27] However, even sophisticated models fail to capture variations in material properties, geometric tolerances, and ill-defined component interfaces.[28, 29] Advances in experimental methods have lagged computational modeling and do not yet provide accurate, real-time measurement of acoustofluidic performance. Available methods often rely on fitting equations for the acoustophoretic motion of passive tracer particles to determine the acoustic energy density, and thus the pressure amplitude. Single-particle tracking (brightfield[30] and holographic time-lapse[31] imaging), microparticle image velocimetry (µPIV),[32, 33] light-intensity

*a. Department of Mechanical Engineering and Materials Science, Washington University in St. Louis, St. Louis, Missouri 63130, USA*

Please do not adjust margins
Lab on a Chip
Page 2 of 13
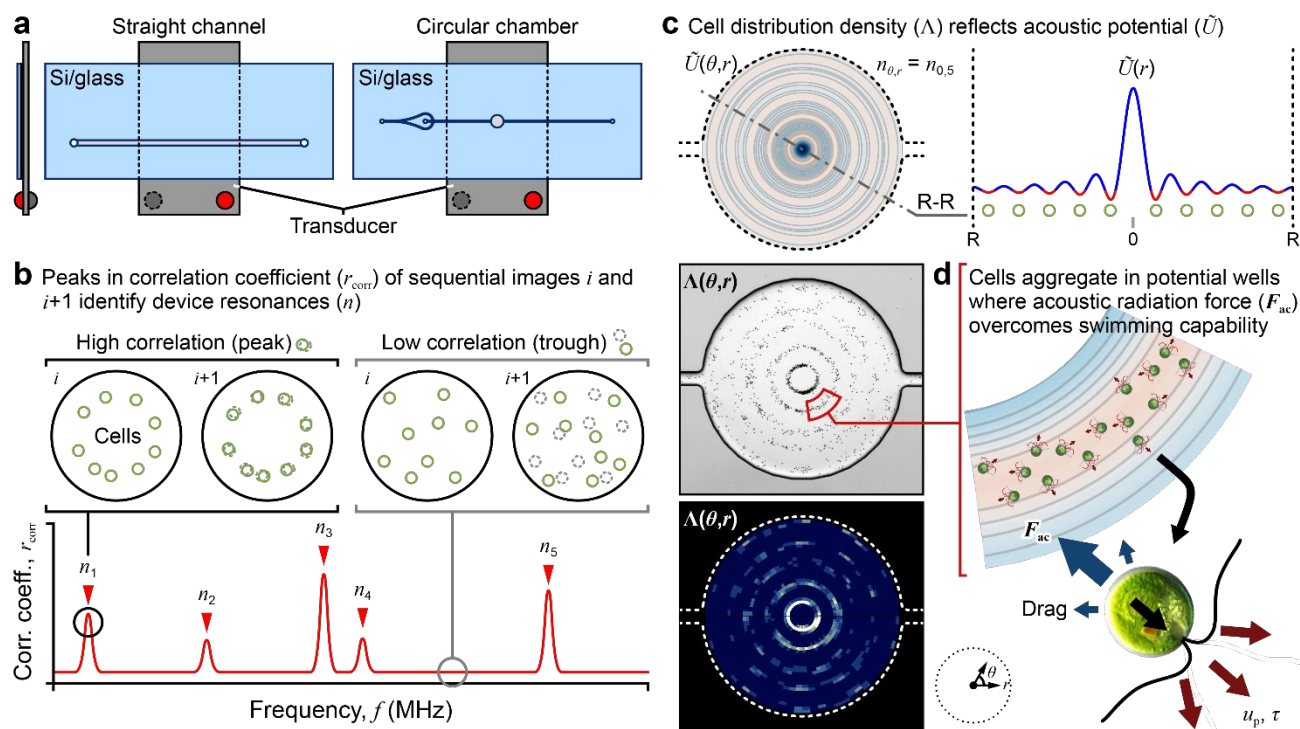
**Fig. 1** Concept for use of *Chlamydomonas reinhardtii* as living acoustofluidic measurement probes: (**a**) simple one- and two-dimensional (1D/2D) acoustofluidic devices for method demonstration/validation, (**b**) image correlation to identify optimal resonant frequencies of operation, (**c**) use of cell density and distribution to form heat maps (light: high density, dark blue: low density) that reflect acoustic potential $\tilde{U}$ (red: negative potential, blue: positive potential) at resonance, and (**d**) the balance of acoustic radiation force $F_{ac}$, drag, and intrinsic swimming capability (represented by swimming speed $u_p$ and reorientation time $\tau$) on a *C. reinhardtii* cell confined to a local potential minimum.

transients,[34] and combined acoustic and optical trapping[35-37] have been reported. These fit-based approaches are limited to simple geometries (e.g., rectangular microchannels or chambers) for which analytical expressions relate the motion of particles to the acoustic radiation force. In addition, continuous monitoring is not possible because inactive particles rapidly reach their terminal positions and cannot redistribute; particles must be refreshed to form a uniform distribution prior to each test condition (drive frequency and/or voltage). Particle-less methods have also been reported;[38, 39] however, their implementation is less straightforward, limiting the utility of these approaches to select research laboratories with unique expertise.

We propose a measurement probe that addresses numerous shortcomings inherent in existing assessment techniques. In the absence of an imposed force field, randomly swimming cells constitute active matter that naturally fills an enclosed volume to create a uniform distribution; however, self-propelled particles (like cells) can become weakly or strongly confined when subjected to an external trap (e.g., optical, magnetic, or acoustic).[25, 40, 41] Active (and reactive) probes also respond to their environment, instantly reflecting changes in the force field as operating or environmental conditions vary. Thus, such active matter can (i) fill complex shapes, (ii) dynamically redistribute as the field changes, (iii) enable continuous monitoring, and (iv) potentially allow field quantification through a force balance on the particles.[41] (i)-(iii) are limited only by the spreading rate of the active matter. The swimming speed of the motile cells used in the present work is

~100 μm/s.[25] Thus, the cells traverse typical microfluidic device channels/chambers in a matter of seconds. Realization of (iv) will require accurate measurement of acoustophysical properties (cell mass density and compressibility) to determine the acoustic contrast factor, in addition to existing knowledge of cell size and swimming speed. Such measurements are the focus of ongoing work.

The biciliate, unicellular alga *Chlamydomonas reinhardtii* (CR) is commonly used as a biochemical and genetic model for studying ciliary diseases in humans (cilia/flagella are propulsive organelles). CR is a model organism. Its characteristics have been studied extensively, and its use in experimental research is routine. Laboratory culture and genetic modification are straightforward, and cell motility is well-characterized as a primary measure of ciliary function. Equally important for the reported work, cells can be prepared in populations with uniform size distribution. When exposed to low-MHz frequency ultrasound, the cell body (~7–8-μm diameter) experiences a trapping force comparable to cell propulsion, while the oscillatory motion of the nanoscale cilia (~200-nm diameter cross section) is only weakly affected. Thus, CR cells continuously swim in a standing acoustic field, such that the balance of propulsive force, acoustic radiation force, and drag prescribes the steady-state distribution of the cells, effectively mapping the pressure field (Fig. 1).

We have previously used an acoustic microfluidic trap to study the impaired motility of mutant CR strains that model human ciliary diseases.[25] In that work, we noted that the apparent trap size could be adjusted up or down using the drive

amplitude. Herein, we introduce a method of adopting CR cells as living probes to measure acoustofluidic device performance. The density and distribution of swimming cells are correlated to the acoustic potential for straightforward identification of device resonances (Fig. 1a,b) and qualitative measurement of field strength (Fig. 1c) throughout the fluidic domains of simple one- and two-dimensional (1D/2D) devices. These living probes provide a more complete description of the evolving pressure field and enable characterization of resonant and off-resonance behavior across a wide frequency spectrum in a single experiment. To our knowledge, this is the first reported method to provide such functionality in real-time and for arbitrarily complex geometries. To demonstrate this utility, we conclude by applying the method to identify the optimal operating frequency of a complex acoustofluidic architecture, overcoming limitations of conventional assessments that are unable to distinguish between proximal device resonances.

## Theory

Here, we develop analytical expressions for the acoustic radiation potential in a 1D straight microchannel and a 2D circular chamber. Table 1 is a list of symbols and abbreviations for reference throughout the theoretical development and to aide in understanding the Results and Discussion.

When an ultrasonic standing wave field develops within a fluid domain, suspended particles are driven to potential minima. For a spherical and compressible particle (radius $a \ll$ wavelength $\lambda$) in an inviscid fluid, the time-averaged acoustic potential $U$ can be expressed as[42]

$$U = 2\pi a^3 \left[ f_0 \frac{\langle p_{in}^2 \rangle}{3\rho_o c_o^2} - f_1 \frac{\rho_o \langle v_{in}^2 \rangle}{2} \right]. \qquad (1)$$

Here, $\rho_o$ and $c_o$ are the fluid density and speed of sound, $p_{in}$ and $v_{in}$ are the first order, oscillating acoustic pressure and velocity at the particle location, and $\langle \rangle$ represents the time average over a full oscillation period of a time-harmonic quantity. Noting that compressibility $\kappa = 1/\rho c^2$, the dimensionless monopole and dipole scattering coefficients $f_0$ and $f_1$ are functions of the ratios of particle (sub p) to fluid (sub o) density and compressibility, $\tilde{\rho} = \rho_p/\rho_o$ and $\tilde{\kappa} = \kappa_p/\kappa_o$, and are given by

$$f_0 = 1 - \tilde{\kappa} \text{ and } f_1 = \frac{2(\tilde{\rho} - 1)}{2\tilde{\rho} + 1}. \qquad (2)$$

The time-averaged force exerted on a particle is then expressed in terms of the gradient of the potential, $\boldsymbol{F}_{ac} = -\boldsymbol{\nabla}U$. We adopt the notation of Barmatz and Collas[43] to define dimensionless radiation potential, force components, acoustic pressure, and particle velocity as

$$\tilde{U} = U/(\pi a^3 \rho_o v_0^2), \qquad (3)$$

$$\tilde{F}_{ac,i} = F_{ac,i}/(\pi a^3 \rho_o v_0^2 k), \qquad (4)$$

$$\tilde{p} = p_{in}/(\rho_o c_o v_0), \qquad (5)$$

| | |
|---|---|
| **Table 1** | List of symbols and abbreviations.* |
| $a$ | particle (cell) radius |
| $c$ | speed of sound |
| $f_0, f_1$ | monopole and dipole coefficients |
| $f^{(\;)}$ | resonant frequency |
| $\boldsymbol{F}_{ac}$ | primary acoustic radiation force |
| $i, m$ | generic counters |
| $k$ | wave number |
| $\kappa$ | compressibility |
| $l, w, h$ | length, width, and height of a rectangular channel |
| $\lambda$ | wavelength |
| $\Lambda$ | particle (cell) distribution density |
| $n$ | channel or chamber resonance |
| $(n_x\, n_y\, n_z)$ | eigenmode of a rectangular channel |
| $(n_\theta\, n_r\, n_z)$ | eigenmode of a circular chamber |
| $\omega$ | circular frequency |
| $p$ | oscillating acoustic pressure |
| $r_{corr}$ | correlation coefficient |
| $R, h$ | radius and height of a circular chamber |
| $\rho$ | mass density |
| $t$ | time |
| $\theta, r, z$ | cylindrical coordinate system of a circular chamber |
| $u_p, \tau$ | intrinsic particle (cell) velocity and reorientation time |
| $U$ | acoustic radiation potential |
| $\boldsymbol{v}$ | oscillating acoustic velocity |
| $v_0$ | maximum acoustic velocity |
| $x, y, z$ | cartesian coordinate system of a rectangular channel |
| sub o | of the fluid |
| sub p | of the particle (cell) |
| tilde ~ | dimensionless or normalized parameter |
| overbar | spatial average |

*Some operators and symbols with derived values are defined within the text of the Theory section.

$$\text{and } \tilde{\boldsymbol{v}} = \boldsymbol{v_{in}}/v_0,$$

where $v_0$ is the maximum acoustic velocity and $k$ is the wavenumber.

For simple chamber geometries, standing wave fields can be described analytically. To demonstrate the proposed method, we first consider a straight microfluidic channel with length $l$, width $w$, and depth $h$ in the $x$-, $y$-, and $z$- coordinate directions, respectively. An eigenmode of the channel (i.e., a field shape that supports a stable particle distribution) is denoted as $(n_x\, n_y\, n_z)$ with $n_x$, $n_y$, and $n_z$ being non-negative integers. Since $l \gg w > h$, the $y$-axial modes $(0\, n_y\, 0)$ are predominant at resonant frequencies $f^{(n_y)}$ in the range of interest (0.5–5.0 MHz), and the resulting 1D wave is given by $\tilde{p}(y,t) = \cos(k_y y)\sin(\omega t)$ using the real-time representation. The acoustic potential then reduces to

$$\tilde{U}(y) = \frac{f_0}{3}\cos^2(k_y y) - \frac{f_1}{2}\sin^2(k_y y), \qquad (7)$$

where the wave number $k_y = \pi n_y/w$.

A circular chamber allows for method validation using more complex 2D standing wave fields. We adopt a cylindrical coordinate system $(\theta\, r\, z)$ and the eigenmode notation $(n_\theta\, n_r\, n_z)$. Again, the mode numbers $n_\theta$, $n_r$, and $n_z$ are non-negative

integers. Since the chamber radius $R$ is much larger than the chamber depth $h$ ($R >> h$), $r$-axial ($0\ n_r\ 0$) and $\theta,r$-tangential ($n_\theta\ n_r\ 0$) modes are predominant at resonant frequencies $f^{(n_\theta,n_r)}$ of interest [again, chamber radius is designed to support low-order ($n_\theta\ n_r\ 0$) modes in the frequency range from 0.5–5.0 MHz]. Under these conditions (i.e., $n_z = 0$), the wavenumber $k_z = 0$, and the dimensionless radiation potential $\tilde{U}$ can be described by a simplified 2D analytical expression in $\theta,r$-coordinates of the circular chamber,[43]

$$\tilde{U}(\theta,r) = \left(\frac{f_0}{3}\right)J_{n_\theta}^2(\chi)\cos^2\left(n_\theta\theta\right) - \left(\frac{f_1}{2}\right)\left[\left(\frac{n_\theta J_{n_\theta}(\chi)}{\chi}\right)^2 + \left(J_{n_\theta}' + \left(\frac{2n_\theta J_{n_\theta}(\chi)}{\chi}\right)\right)\cos^2\left(n_\theta\theta\right)\right] \tag{8}$$

where $\chi = k_r r$, $k_r = \pi\,\alpha_{n_\theta,n_r}/R$, and $J_{n_\theta}$ is the Bessel function of order $n_\theta$. For rigid boundary conditions, $\pi\,\alpha_{n_\theta,n_r}$ is a root of the derivative of the Bessel function.

The expressions for the acoustic radiation potential in a 1D straight channel and a 2D circular chamber [Eqs. (7) and (8), respectively] provide test cases for our field mapping approach. We have chosen to map acoustic potential (instead of pressure) because in 2D standing wave fields, pressure nodes do not necessarily coincide with potential minima.[43, 44] CR cells suspended in our devices will feel an acoustic restoring force toward the radiation potential wells. In addition, potential wells in the circular chamber are not symmetric in $r$, allowing observation of different cell distribution density gradients along directions of stronger and weaker restoring forces, i.e., assuming propulsive capability is uniform, cells will spread out more in the direction of a weaker potential gradient. Finally, these analytical descriptions identify observed resonances. Importantly, it is also possible to determine which mode shapes are *not* driven efficiently by the system as these eigenmodes will not be exhibited by the cell distribution.

Our theoretical treatment assumes that the primary acoustic radiation force and swimming force are dominant over the secondary acoustic radiation force and Stokes drag arising from acoustic streaming. Secondary (interparticle) forces can confound measurement of the acoustic potential using passive particles, due to their nonuniform initial distribution (i.e., variation in particle-particle separation) and tendency to aggregate at nodal locations over time.[45-47] Secondary forces become important very near pressure nodes and for short-range interactions (e.g., separation distances less than approximately two particle radii[46]). In the present work, the cilia apparently prevent swimming cells from closely approaching one another. Even as CR cell populations become tightly confined to acoustic potential minima, we observe cells swimming freely perpendicular to the wave propagation direction. Only the few immotile (e.g., dead) cells in the population are seen to aggregate. Thus, neglect of secondary acoustic radiation forces is justified.

The relative importance of acoustic streaming and radiation forces in acoustic manipulation of micrometer-sized particles has been thoroughly investigated.[33, 48] Barnkob et al.[33] defined the critical radius $a_c$ below which a shift from radiation- to streaming-dominated acoustophoresis occurs, which was ~1 μm for polystyrene (PS) microparticles suspended in water.

Although the acoustic contrast factor of CR cells is smaller than that of PS beads (and therefore $a_c$ is slightly larger), we do not expect the ~8-μm diameter cells to approach the corresponding threshold size. Indeed, once the cells reach a steady distribution density, we do not observe a rectified motion of the swimming cells that might indicate significant effects of streaming.

## Materials and Methods

### Fabrication and assembly of acoustofluidic devices

Acoustofluidic chips were fabricated using conventional micro-fabrication processes.[2] Two-step anisotropic deep reactive ion etching (DRIE; front side channel, ~49-μm depth; back-side inlet/outlet, through) was used to create fluidic layers with a straight channel ($l$ = 30 mm, $w$ = 0.75 mm) and circular chamber ($R$ = 1.8 mm) in 300-μm thick silicon wafers. The fluidic layer was enclosed with a 500-μm thick Borofloat® 33 cover glass using anodic bonding. The microfluidic chip was diced to a final size of 40 mm × 16 mm. A 14 mm × 24 mm × 0.75-mm thick PZT-8 piezoelectric transducer (APC 880, American Piezo Ceramics, Inc.) was epoxied to the back side of the Si-glass chip centered between the inlet/outlet ports (see Fig. 1a).

An Si-glass chip incorporating a more complicated fluidic architecture was fabricated using a similar protocol. The ultrasonic MIcroarray Spray Tuning (uMIST) chip geometry was designed to approximate the acoustic behavior of a 3D ultrasonic atomizer with pyramidal nozzles in 2D and with visual access.[27, 49] The fluidic layer comprised curved inlet/outlet channels and a rectangular fluid reservoir bounded on one edge by a linear array of six triangular features. Channels were etched in 500-μm thick silicon to a depth of 200 μm. The microfluidic chip, an aluminum coupling layer (24 mm × 24 mm × 3-mm thick), and a PZT-8 piezoelectric transducer (24 mm × 28 mm × 1.5-mm thick) were assembled into a custom microscope stage insert using mechanical clamping. Ultrasound gel (McKesson Corp.) was applied in between the components to improve system coupling [for a complete description of computational modeling and experimental assessment of the uMIST chip using passive PS beads see Ledbetter et al.[27]].

### Cell culture and sample preparation

Wild-type *Chlamydomonas reinhardtii* cells (CR, strain CC-125) were obtained from the Dutcher Lab at Washington University in St. Louis and prepared as previously reported.[50] Briefly, cells were grown on agar plates at 25°C under constant lighting for 48 hrs. After incubation, the agar plates were stored at room temperature. Before an experiment, cells from the agar plate were resuspended in a liquid growth medium for three hours for cilia growth. A growth medium that lacked nitrogen was used to promote gametogenesis, which helped to increase the number of motile cells and achieve a higher size uniformity. The cell sample was then centrifuged at 1000 g for 5 min and the sample volume was adjusted to achieve a concentration of ~$10\times10^6$ cells/mL.

Page 5 of 13
Please do not adjust margins
Lab on a Chip

## Video microscopy

Cell movement in microfluidic channels was observed using 2.5X and 5X objectives (EC Plan-Neofluar 2.5x/0.085 M27 and 5x/0.16 M27, Zeiss) on an inverted microscope (Axio Observer z.1, Zeiss). Image acquisition was done using a 3-Megapixel camera and imaging software (Axiocam 503; ZEN software, Zeiss). The pixel resolution was 1932 × 1460: 1.82 µm × 1.82 µm/pixel for 2.5X and 0.91 µm × 0.91 µm/pixel for 5X. The frame rate was set to 5 fps for all videos.

## Frequency and voltage control

For automatic identification of device resonant frequency(ies), the actuation frequency was swept from 500 kHz to 5.0 MHz at 10-kHz intervals for the straight channel and circular chamber, and from 1.5 MHz to 2.0 MHz for the uMIST chip (33522A, Agilent; 2100L, ENI). Actuation was held for 1.5 s at each frequency step. The impedance response of the loaded piezoelectric element was determined by measuring the applied voltage waveform (using a voltage probe at the piezoelectric element), the current waveform (voltage probe across a ground-side current sensing resistor), and phase (relationship between the two waveforms) over the relevant frequency range of interest using a PC oscilloscope (PicoScope 2204A; Pico Technology). Measurements were used to adjust the waveform generator input voltage at each frequency step to achieve a constant peak-to-peak output voltage throughout the frequency sweep.

For the field strength mapping, the frequency was held constant while increasing the voltage from zero at ~1 $V_{pp}$ increments for the straight channel and ~0.4 $V_{pp}$ increments for the circular chamber. Actuation was held for 10 s at each voltage step. Since the ideal temperature range for CR cells is 20°C to 32°C,[51] all experiments were performed on a temperature-controlled (20°C) stage insert (PE100, Linkam) to retain high cell viability. Consistent temperature is also needed to ensure reliable and reproducible acoustofluidic device performance. Temperature control ensures that long-term device actuation does not lead to device heating. Prolonged exposure to an applied acoustic field does not lead to a loss of cell function or viability as long as the temperature remains below ~38°C.[25]

## Image processing and analysis

The waveform generator was controlled via Python,[52] and a timestamp was logged at each frequency/voltage step. The timestamps were aligned with the image acquisition time to identify the operating parameters for each image. For identification of the device resonances, a grayscale image was recorded at each operating frequency step. The correlation coefficient of successive images was calculated using the *corr2* function in MATLAB,[53] which determines the similarity of two images based on the intensity at each pixel location relative to the mean intensity of each image. The resulting correlation coefficient was plotted against the drive frequency. Near a device resonance, cells became confined to potential minima; the cell distribution was relatively unchanged from image to

image, and the correlation coefficient was elevated. Away from resonance, cells swam freely; cell positions constantly changed, and the correlation coefficient was low. Each frequency sweep was repeated a minimum of four times (straight channel: $m = 5$ repeats; circular chamber: $m = 7$; uMIST chip center: $m = 6$; uMIST left/right domains: $m = 4$).

To generate color maps of cell distribution, brightfield images obtained during the voltage sweep were converted to binary (black/white) and the number of black pixels (areas occupied by cells) from 50 images at the same voltage level was summed. The shadowed regions adjacent to channel and chamber walls were excluded. Rectangular bins of 27.3 µm × 27.3 µm were used for the straight channel field mapping. For the circular chamber, radial bins with radius 27.3 µm and angle π/36 rad were used. Pixel counts for each radial bin were divided by the area of the bin to account for the different bin sizes. After determining the minimum and maximum densities for an experiment (i.e., the lowest black pixel count observed for a vacant bin near the potential maximum at high voltage, and the highest count for a bin near the potential minimum), the cell distribution densities for each bin (and at each voltage) were normalized. Distribution maps were generated by assigning a color to each of seven linearly distributed density ranges (sequential scientific color-map *davos*;[54] light: high density, dark blue: low).

# Results and discussion

## *C. reinhardtii* cells as living probes of acoustofluidic performance

Conventional acoustic microfluidic device assessments rely on the consistency of the acoustophysical properties of passive particles; tracer particles must be uniform in size, density, and compressibility. Polymeric microspheres with extremely uniform sizes are widely available from submicron to tens of microns in diameter. Many biological cells are not well-suited to this purpose as individual cells in a culture exist at different stages of the cell-division cycle (and thus, exhibit a heterogeneous size distribution). Vegetative CR cells are easily driven to differentiate into haploid gametes by suspension in nitrogen-depleted medium. Here, we use CR cells of a single mating type to ensure that mature gametes cannot fuse. This halts the cell life cycle to synchronize the cell population for acoustofluidic performance measurements. The CR cells exhibit a uniform size and swimming effectiveness across a given strain (diameter = 8.0 ± 1.1 µm, $n$ = 138; swimming speed is approximately 100 micrometer per second for strain CC-125).[25, 55, 56]

CR cells are vigorous swimmers that naturally maintain an even distribution within a liquid-filled enclosure. In the absence of an imposed force field, individual cells can traverse the characteristic length (e.g., the channel width) of a typical microfluidic device in a few seconds. Cells continue to swim within an ultrasonic standing wave field; however, the acoustic radiation force influences their motion (see Theory). Cells are confined within an acoustic potential well when the local radiation force exceeds the propulsive capability of the cells at the trap

Please do not adjust margins
Lab on a Chip
Page 6 of 13

**a** Identified straight channel resonant frequencies $f^{(n_y)}$ corresponding to half-wavelength modes $n_y$
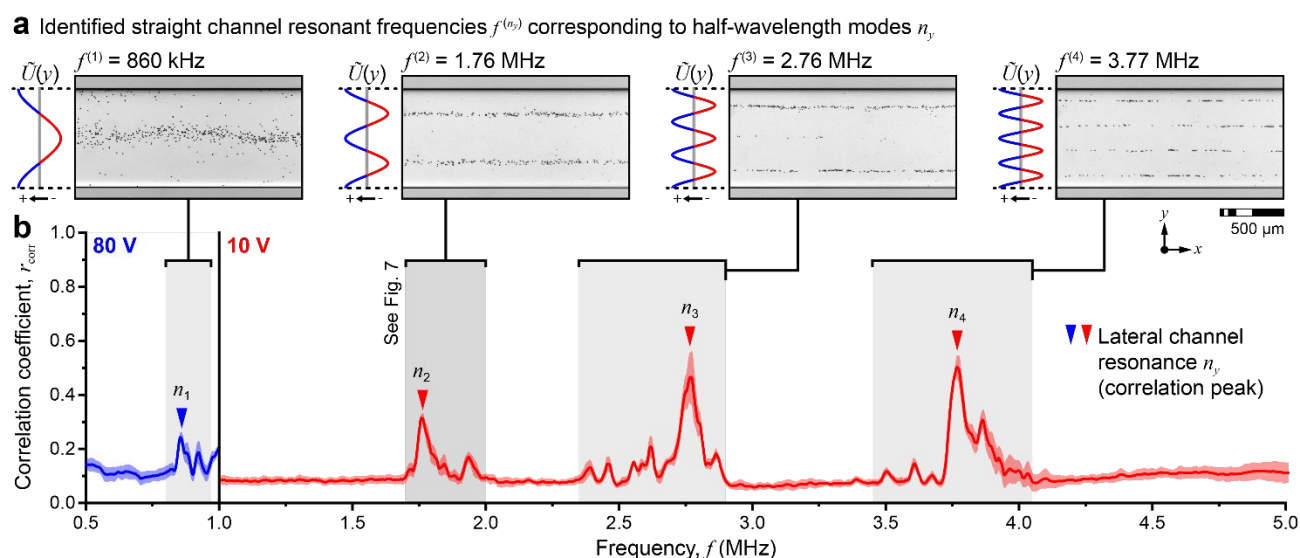


**Fig. 2** Resonance identification for the straight microfluidic channel: (**a**) brightfield microscopy of CR cell distributions shows cells collecting at potential minima of the first four half-wavelength resonances in the lateral ($y$-) direction, and (**b**) peaks in the correlation coefficient for successive images easily identify these resonant frequencies. Data represent $m$ = 5 sequences and are plotted as mean values +/- s.d.

boundary. As the field strength increases, the accessible region of the potential well becomes smaller, and cells become more tightly packed. Thus, the density and distribution of cells within a channel or chamber reflect the shape and strength of an evolving acoustic field. The propulsive force is intrinsic to a cell strain. We used wild-type CR cells (strain CC-125) in the present study, but CR mutants with impaired motility could be used to characterize weaker fields that are unable to confine CC-125.

**Automatic identification of device resonances**

Figure 1 illustrates the application of CR cells as active probes to characterize an ultrasonic standing wave field. Si-glass micro-fluidic chips with simple 1D and 2D geometries (Fig. 1a) were used to demonstrate two different measurements: (i) resonance identification (Fig. 1b), and (ii) qualitative mapping of the acoustic field strength (Fig. 1c). First, we show that the CR cell distribution as a function of swept frequency can be used to automatically detect device resonances within a prescribed frequency range. At off-resonant frequencies, the correlation coefficient between successive images is low as cells navigate the entire fluid domain, and their positions continuously vary from image to image. At resonance, the acoustic field strength increases, and cells become confined to the potential minima. The invariant locations of higher cell concentration result in a high image correlation, which is easily observed in the data.

**Straight channel (1D ultrasonic standing wave).** After seeding the straight microfluidic channel with CR cells, the drive frequency was swept from 500 kHz to 5.0 MHz. The drive voltage was maintained at 80 $V_{pp}$ from 500 kHz to 1.0 MHz and at 10 $V_{pp}$ from 1.0 MHz to 5.0 MHz. We initially held the drive voltage constant at 10 $V_{pp}$ throughout the entire frequency range; however, inefficient actuation (e.g., due to poor coupling of vibrational and acoustic waves) over the lower frequency range necessitated a higher-amplitude signal to observe the first half-wavelength resonance.

As expected, most prominent potential minima developed along the lateral ($y$-) direction at frequencies that correspond to multiples of the half-wavelength equal to the channel width [$y$-axial modes (0 $n_y$ 0); see Theory]. For resonant frequencies $f^{(n_y)}$, $n_y$ lateral potential minima lines developed as shown in Fig. 2a [note that potential line plots $\tilde{U}(y)$ are determined using Eq. 7]. The variation in correlation coefficient of successive images as a function of the drive frequency is shown in Fig. 2b. Resonant frequencies exhibited peaks in correlation coefficient [$f^{(1)}$ = 860 kHz, $f^{(2)}$ = 1.76 MHz, $f^{(3)}$ = 2.76 MHz, and $f^{(4)}$ = 3.77 MHz; see Supplementary Movie S1]. Between these resonances, CR cells evenly redistributed throughout the fluid domain. Thus, image correlation provides a quantitative method for automated experimental identification of optimal operating frequency(ies) within a frequency range of interest.

We also identified weaker device resonances as smaller peaks in the correlation coefficient [see Fig. 3 for detailed analyses of frequency bands around $f^{(1)}$ and $f^{(3)}$]. Cells quickly dispersed to form a uniform distribution after confinement at the $n_1$ resonance. Consequently, the correlation coefficient dropped to a baseline value at $f$ = 900 kHz. Shortly thereafter, cells aggregated in bands along the channel length ($x$-) direction at $f^{(1a)}$ = 928 kHz, suggesting that a semi-stable longitudinal resonance [i.e., an ($n_x$ 0 0) mode] existed at this frequency. Several weaker resonances appeared in the $n_3$ range as well. As the drive frequency approached this resonance, two longitudinal [$f^{(3a)}$ = 2.39 MHz and $f^{(3b)}$ = 2.46 MHz] and two lateral resonances [$f^{(3c)}$ = 2.55 MHz and $f^{(3d)}$ = 2.61 MHz] were observed before the most stable device resonance developed at $f^{(3)}$ = 2.76 MHz. Another minor resonance was identified slightly above the $n_3$ resonance at $f^{(3e)}$ = 2.86 MHz. At this frequency, CR cells formed three distinct horizontal lines that extended from the left approximately halfway across the field of view in the $x$-direction, at which point the lines dispersed into an even cell distribution. These behaviors are indicative of real-
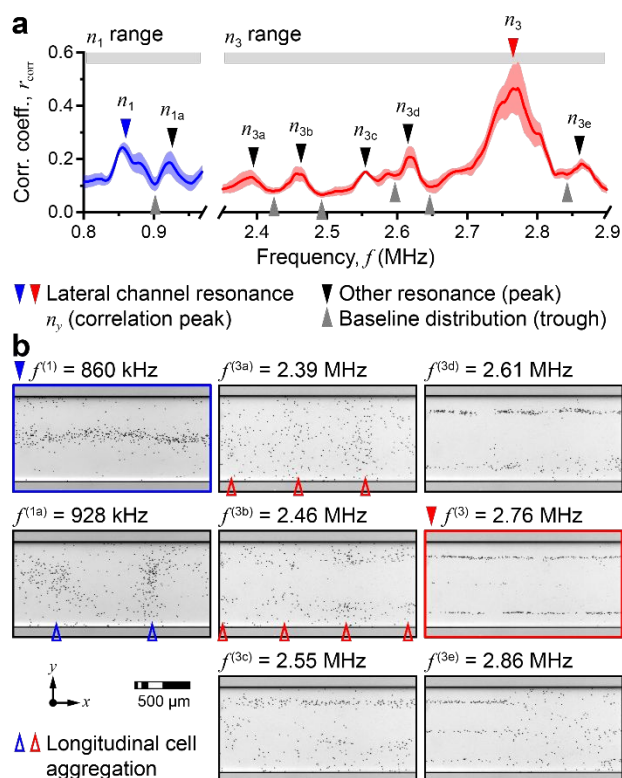
**Fig. 3** Off-resonance behaviors: (**a**) identification of minor peaks and troughs (i.e., returns to baseline distribution) in the vicinity of the first and third lateral (y-direction) half-wavelength resonances, and (**b**) CR cell distributions at identified resonances. Data represent $m$ = 5 sequences and are plotted as mean values +/- s.d.

world irregularities in material properties or device construction (coupling layers, asymmetry, etc.) and may vary from device-to-device. Such shapes are either difficult or virtually impossible to predict using computational models.

**Circular chamber (2D ultrasonic standing wave).** As with the straight microchannel, device resonances of the circular chamber were identified using CR cells. The drive frequency was swept from 500 kHz to 1.5 MHz at a drive amplitude of 60 $V_{pp}$ and from 1.5 MHz to 5.0 MHz at 10 $V_{pp}$. Here, peaks in image correlation successfully identified various $r$-axial and $\theta,r$-tangential resonances of the chamber (Figs. 4 and 5, and Supplementary Movie S2). Figure 5 overlays the corresponding cell distributions on analytical solutions $\tilde{U}(\theta,r)$ for the potential field of a circular chamber at resonance (see Eq. 8). The 2D contour ("a") and 1D line ("b") plots in Fig. 5 indicate the relative depth (height) of the local potential minima (maxima) for each case [divergent scientific color map vik;[54] red: negative potential (minima), blue: positive potential (maxima)]. Cell locations are shown as black dots.

Due to field instability in the 0.5–1.5 MHz range, cells did not return to a completely even distribution between peaks in image correlation. Hence, we observed a series of minor peaks without the correlation coefficient returning to its baseline value (see Supplementary Movie S2). One of these smaller peaks [$f^{(0,1)}$ = 755 kHz] resembled the first $r$-axial mode. Other peaks were not easily identifiable as solutions of Eq. 8. We detected four major peaks in the 1.5–5.0 MHz frequency range. The (0 $n_r$ 0) $r$-axial modes correspond to shapes characterized by potential minima 'rings'; $f^{(0,1)}$ = 755 kHz, $f^{(0,3)}$ = 2.54 MHz, and $f^{(0,5)}$ = 4.25 MHz displayed one, three, and five rings, respectively (see Figs. 4a and 5a). The mode number $n_\theta$ introduces an angular dependence that gives rise to potential minima 'diameters'. When $n_\theta$ > 0, more complex 2D field shapes developed for the $\theta,r$-tangential modes observed at $f^{(2,1)}$ = 1.66 MHz and $f^{(3,2)}$ = 2.86 MHz (Figs. 4a and 5a).

The peak centered around $f$ = 2.5 MHz exhibits an interesting interplay between two chamber resonances. As the correlation coefficient increased with increasing frequency, we observed two resonances [($n_\theta n_r$ 0) = (2 2 0) and (0 3 0)] and
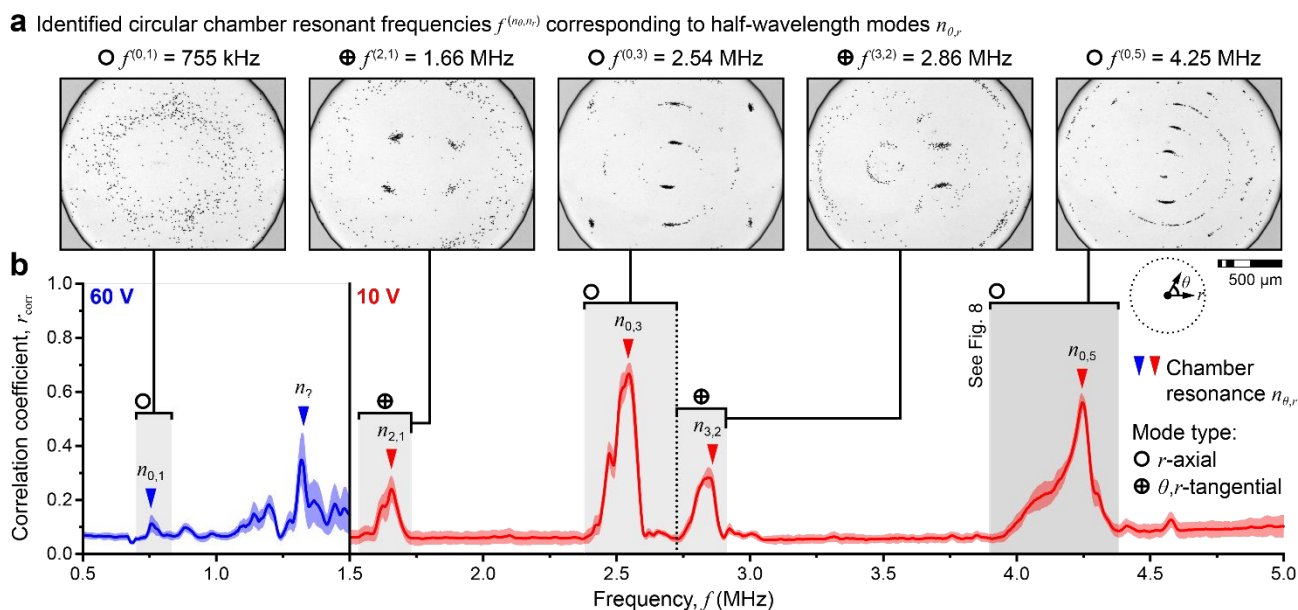


**Fig. 4** Resonance identification for the circular chamber: (**a**) CR cell distributions for observed $r$-axial and $\theta,r$-tangential resonances, and (**b**) the corresponding peaks in the image correlation coefficient. Data represent $m$ = 7 sequences and are plotted as mean values +/- s.d.

Please do not adjust margins
Lab on a Chip
Page 8 of 13

**a** Analytical solutions for the normalized acoustic potential $\tilde{U}$ at circular chamber resonant frequencies $f^{(n_\theta, n_r)}$



**b**
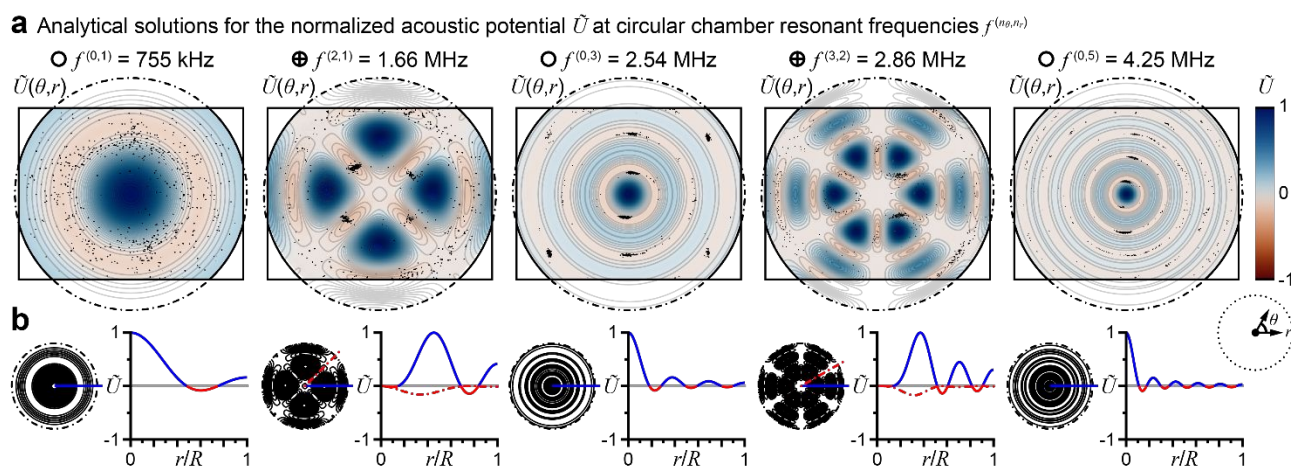


**Fig. 5** Comparison of CR cell distributions and analytical expressions (Eq. 8) for the mode shapes of a fluid-filled circular chamber: (**a**) overlay of cells (black dots) on 2D contour plots, and (**b**) 1D line plots indicating the relative depth (height) of the local potential minima (maxima) (note that 2D and line plots are normalized to the maximum value for each case).

multiple transitional patterns without reversion to the baseline distribution. The CR cells alternated between distributions resembling these two eigenshapes, first achieving a (0 3 0) shape at $f^{(0,3c)}$ = 2.46 MHz, then (2 2 0) at $f^{(2,2)}$ = 2.50 MHz, before reaching a maximum in correlation coefficient at $f^{(0,3)}$ = 2.54 MHz (see Fig. 6 and Supplementary Movie S3). Slight field rotations were also seen; however, angular variations are not surprising due to an absence of reflecting boundaries for cylindrical (i.e., in $\theta$) waves. (note Eq. 8 assumes an arbitrary phase constant $\theta_0$ = 0).[43] Real-time video of this frequency range (Supplementary Movie S3) also reveals how key experimental parameters might be adjusted to gain additional insight into device behavior. The image sequence permits identification of two distinct mode shapes; however, the rapid evolution of the field does not allow cells to revert to a baseline distribution in between the resonances. If finer resolution is required, smaller frequency steps, longer hold times, and/or zero voltage reversions between steps are easily implemented in the protocol.

### Qualitative mapping of the acoustic field strength

The pattern of the CR cell distribution identifies the resonance by mode shape. In addition, the spread of CR cells that form the pattern reflects the acoustic field strength, which depends on the drive voltage at a fixed frequency.

**Second half-wavelength resonance of the straight channel (1D ultrasonic standing wave).** The field strength was characterized using a voltage sweep performed at the second half-wavelength resonance of the straight channel $f^{(2)}$ = 1.76 MHz. The voltage was linearly increased from 0 to 20.6 $V_{pp}$ at increments of ~1 $V_{pp}$. Figure 7a shows representative brightfield images of the channel, along with distribution maps generated from 50 consecutive images taken at each voltage (note that only every-other voltage increment is shown, starting at the subthreshold voltage for CR cell confinement and ending at the saturation voltage beyond which no further confinement occurred). The normalized acoustic potential $\tilde{U}(y)$ is plotted to indicate the
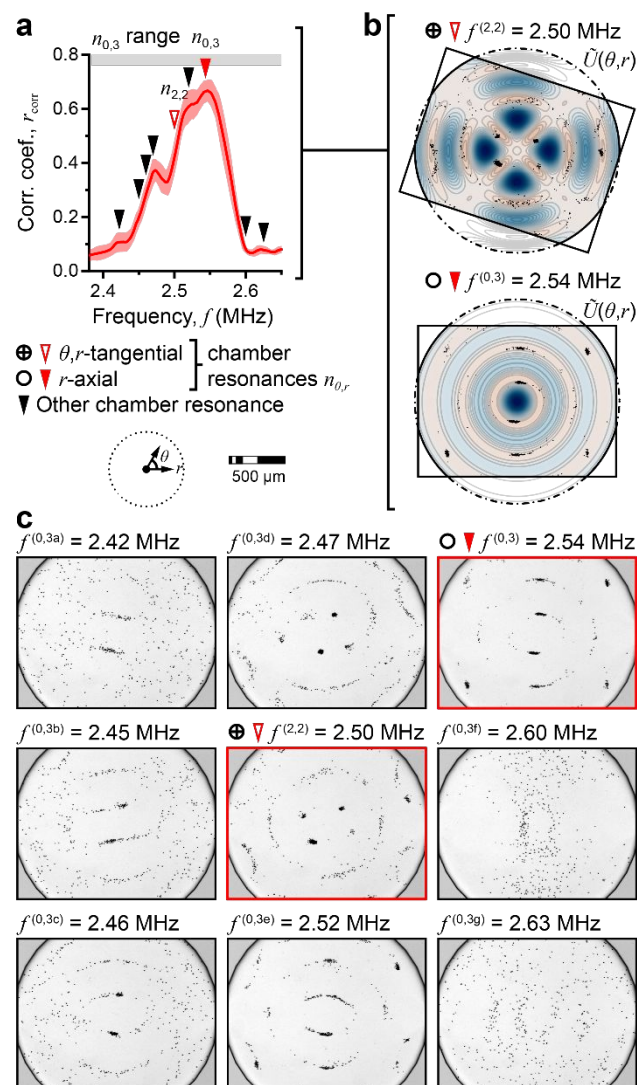


**Fig. 6** Multi-resonance peak identification: (**a**) the $n_{0,3}$ range includes a compound peak comprising (**b**) two major resonances [$(n_\theta\, n_r\, 0) = (2\, 2\, 0)$ and $(0\, 3\, 0)$] and (**c**) several transitional patterns without reversion to the baseline distribution. Data represent $m$ = 7 sequences and are plotted as mean values +/- s.d.

ARTICLE
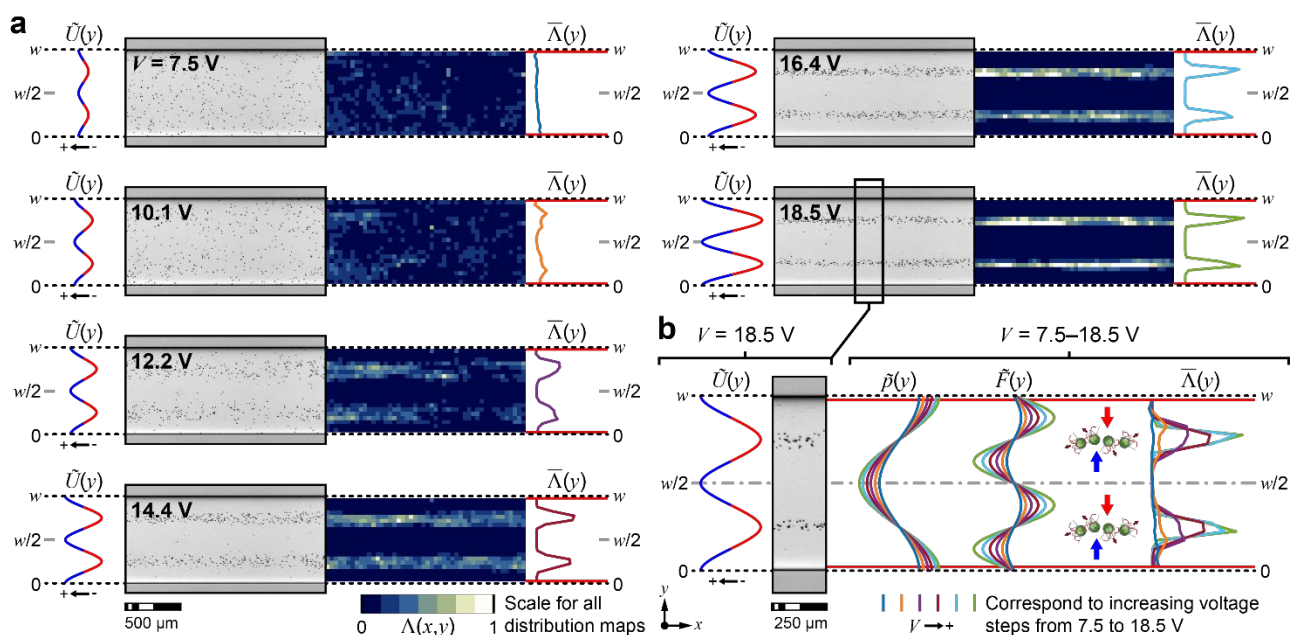


**Fig. 7** Qualitative mapping of the acoustic field strength for the second half-wavelength resonance of the straight microfluidic channel: (**a**) acoustic potential line plots, brightfield microscopy, distribution maps, and line plots of the CR cell distribution density averaged along the channel segment with increasing drive voltage, and (**b**) normalized potential, pressure, and acoustic radiation force in the lateral ($y$-) direction to illustrate how variations in the acoustic trap parameters relate to the evolving distribution of swimming cells (note line plots are normalized to the maximum value for the highest voltage case).

positions of the potential wells. Plots of the experimentally determined cell distribution density averaged along the channel segment $\overline{\Lambda}(y)$ are included for comparison with the potential line plots.

The CR cells continuously responded to the evolving acoustic field. At low voltages, cells navigated the entire channel, but as the voltage was increased, the influence of the acoustic field on the cell motion became apparent (see Supplementary Movie S4). After exceeding a threshold voltage of ~12 $V_{pp}$, cells were confined to two horizontal bands corresponding to the regions of potential minima. With a further voltage increase, cells explored smaller areas creating tighter and higher peaks in the cell distribution density. Thus, cell confinement is a function of actuation voltage (and acoustic field) amplitude.

Figure 7b includes normalized pressure and normalized acoustic radiation force in the $y$-direction, along with the normalized acoustic potential and experimental cell distribution density measurements compiled for the voltage increments in Fig. 7a. Here, the regions where the CR cells were confined corresponded to the acoustic pressure nodes (pressure minima). The acoustic radiation force ($\boldsymbol{F}_{ac} = -\boldsymbol{\nabla}U$) was zero at these nodes, and the acoustic trap was bounded by a threshold radiation force that the cells could not overcome. The spatial location of this threshold for cell confinement is voltage and cell-strain dependent; larger voltages would generate a stronger field, and cells with impaired motility would exhibit weaker swimming strength.

**Fifth $r$-axial resonance of the circular chamber (2D ultrasonic standing wave).** Field strength experiments were repeated for the circular chamber by sweeping the drive voltage at the fixed

frequency $f^{(0,5)} = 4.23$ MHz, which corresponded to the (0 5 0) $r$-axial mode. Five rings gradually materialized as the voltage was increased from 0 to 10.6 $V_{pp}$ (see Fig. 8a and Supplementary Movie S5; again, every-other voltage increment is shown; the image sequence stops at the saturation voltage $V = 5.9$ $V_{pp}$). The central region of the chamber was cleared first, becoming devoid of CR cells at $V = $ ~2 $V_{pp}$. The inner rings then developed during the period from ~2 $V_{pp}$ to 4 $V_{pp}$. Finally, the outer rings appeared from ~4 $V_{pp}$ onward, though an angular dependence arose within the pattern before the ring structure was complete. We observed that the cells were more densely packed in the inner rings as predicted by the analytical expression for the radiation potential $\tilde{U}(\theta, r)$ (Eq. 8), which is plotted next to a sector of the chamber image in Fig. 8b. Cells were positioned within potential minima, which coincided with acoustic radiation force nodal regions. Note that the terminal distribution also appeared to align with the pressure nodal regions; however, this is not actually the case as $r$-axial nodal surfaces are dependent on the sample properties (through dimensionless coefficients $f_0$ and $f_1$) for this geometry.[43, 44] Without measurements of the acoustophysical properties of the CR cells, we assumed values for density and compressibility ($\rho_p = 1100$ kg/m³ and $\kappa_p = 300 \times 10^{-12}$ Pa⁻¹) as the average of a typical mammalian cancer cell and a plant cell to resolve expressions for acoustic pressure, radiation potential, and radiation force. While these assumptions likely introduced error in the analytical solutions, we found that predicted fields were not appreciably different when using values for any of these three cell types. Despite the limitations due to uncertain parameter values, these results demonstrate the utility of CR cells to enable qualitative comparison of field strength for

Please do not adjust margins
Lab on a Chip
Page 10 of 13
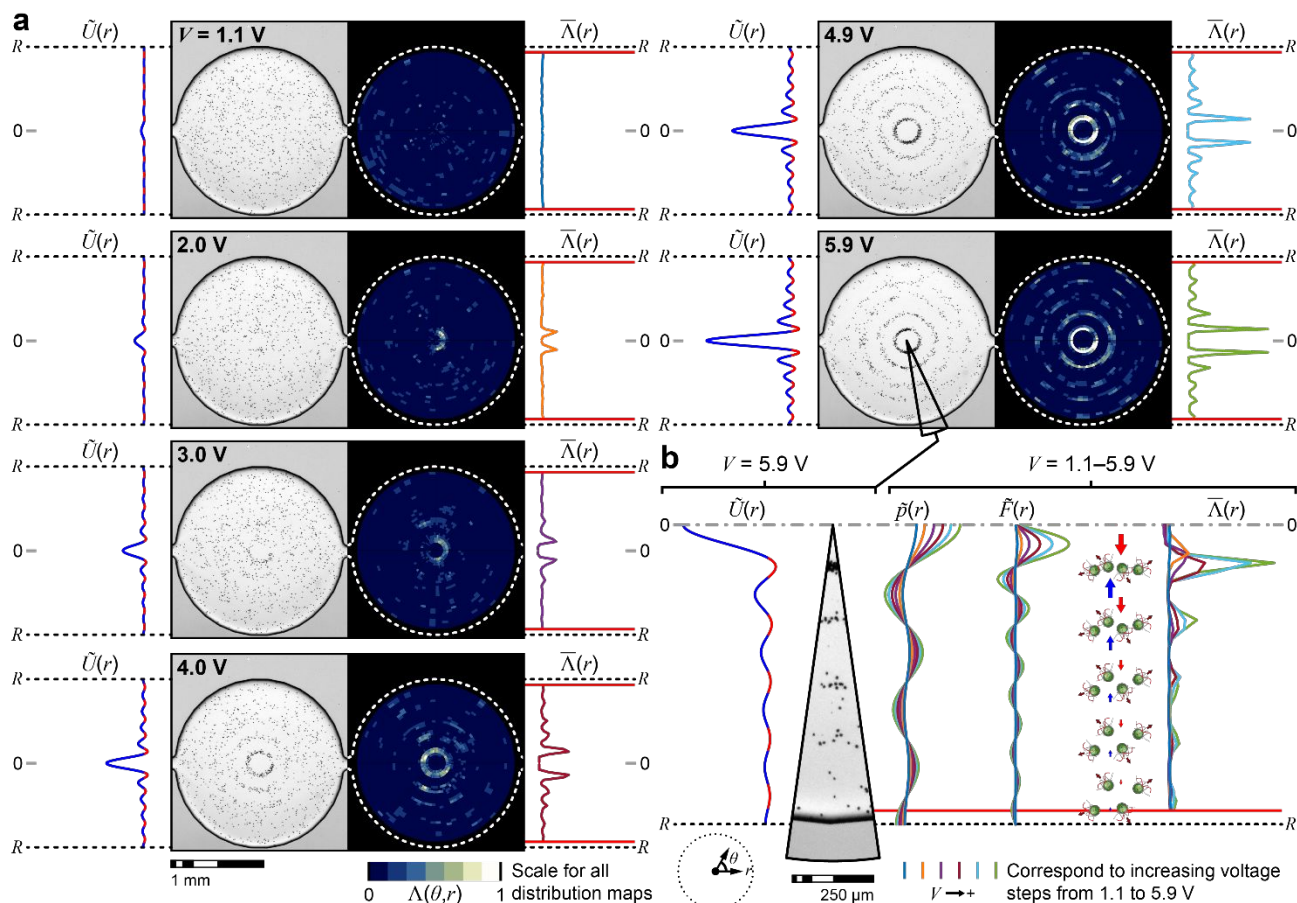
**Fig. 8** Qualitative mapping of the acoustic field strength for the (0 5 0) $r$-axial resonance of the circular chamber: (**a**) acoustic potential line plots, brightfield microscopy, distribution maps, and line plots of the CR cell distribution density (averaged by summing normalized bin counts at each radial position) with increasing drive voltage, and (**b**) normalized potential, pressure, and acoustic radiation force in the radial ($r$-) direction to illustrate how variations in the acoustic trap parameters relate to the evolving distribution of swimming cells (note line plots are normalized to the maximum value for the highest voltage case).

different input power levels. This capability should also be applicable to device-to-device performance assessments.

**Characterization of a device with complex geometry**

In the preceding sections, we have introduced our method using simple 1D and 2D geometries. Here, we demonstrate the ability of CR cells to assess performance of a complex resonant acoustofluidic device that has previously been studied using finite element analysis (FEA) and focusing of passive polystyrene (PS) beads.[27] The uMIST chip comprises two contiguous fluidic regions: (i) a central chamber with a linear array of six triangular features ('nozzles'), and (ii) symmetrical regions with expanding/contracting curved microchannels connecting the central chamber to the sample inlet/outlet [labeled "Left" ("L") and "Right" ("R") in Fig. 9b,c]. Ideal operating frequencies exhibit longitudinal ($z$-direction) ultrasonic standing waves that are focused to a high maximum pressure at the nozzle tips. These resonances are termed 'ejection modes' as they correspond to effective droplet generation from a 3D ultrasonic atomizer.[27, 49, 57] The device has multiple ejection modes within the operating frequency range of interest (0.5–5.0 MHz), which makes resonance identification using passive particles a challenge.

A 2D multi-domain FEA model comprising the piezoelectric element ("PZT" in Fig. 9b), an aluminum coupling layer ("Al"), silicon chip ("Si/Glass"), and the liquid sample was used to develop design principles for component geometry regarding efficient operation (see Fig. 9d-f).[27] Model validation was laborious as PS bead solutions had to be reloaded to observe the evolving field as drive frequency was adjusted in the vicinity of the predicted resonances. Though the FEA model provided useful insight into device operation, its predictive power was limited by use of reference (versus measured) material properties, idealized interfaces, and perfect assembly.

*In situ* device assessment using CR cells overcomes the shortcomings of FEA. As before, CR cells were loaded prior to actuation, forming a uniform distribution throughout the sample chamber. The field shapes were then continuously monitored as the frequency was swept from 1.5 MHz to 2.0 MHz at 45 $V_{pp}$. Images were acquired and separately analyzed for the three chamber regions shown in Fig. 9c. Image correlation was used to identify potential resonances of interest.

The results shown in Fig. 9 highlight several advantages of using active probes for experimental assessment of acoustofluidic devices. Both the FEA model and passive particles suggest that the optimal operating frequency displays mixed
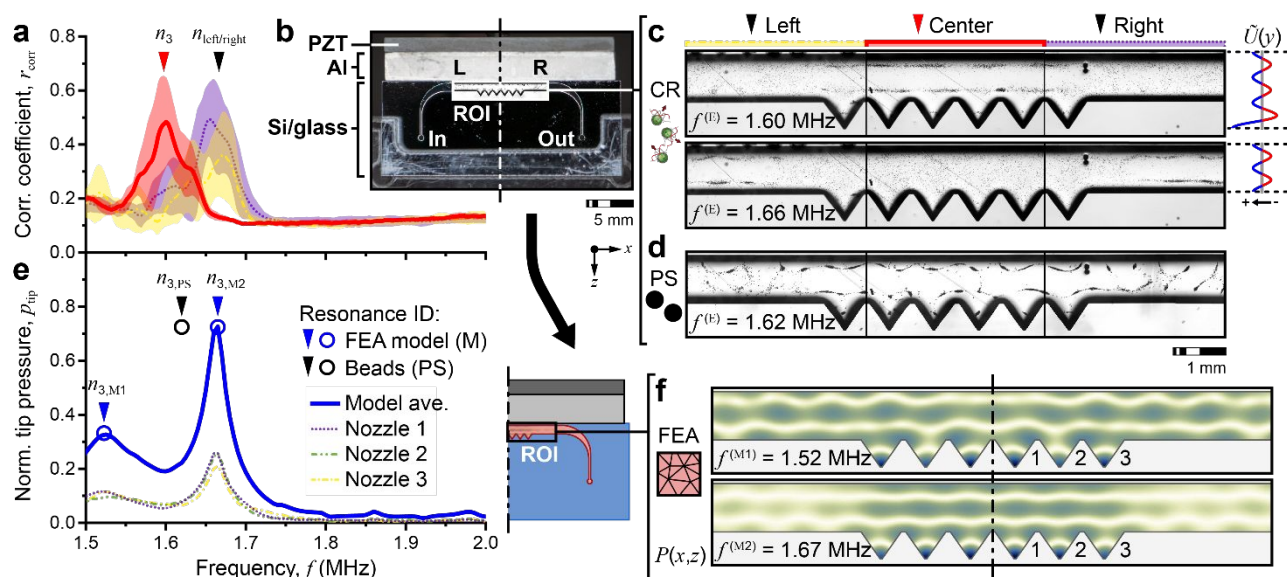
**Fig. 9** Dynamic performance characterization of the complex uMIST channel geometry for the continuously swept frequency range from 1.5–2.0 MHz: (**a**) peaks in image correlation identify resonances of the central nozzle region (red, $n_3$; data represent $m = 6$ sequences and are plotted as mean values +/- s.d.) and lateral left (L)/right (R) regions (yellow dashed-dotted and purple dotted, $n_{left/right}$; data represent $m = 4$ sequences and are plotted as mean values +/- s.d.); (**b**) 2D chip assembly with actuation along the top (-$z$) edge; (**c**)-(**d**) brightfield microscopy of experimental channel resonances observed using CR cells ["c", $f^{(E)} = 1.60$ and 1.66 MHz] and polystyrene beads ["d", $f^{(E)} = 1.62$ MHz]; (**e**) model-predicted device harmonic response suggesting that multiple ejection modes ($n_{3,M1}$ and $n_{3,M2}$) fall within the frequency range of interest; and (**f**) contour plots of the FEA-predicted device resonances [$f^{(M1)} = 1.52$ MHz and $f^{(M2)} = 1.67$ MHz].

behavior with pressure nodal regions (and particle focusing) observed within both the central chamber and inlet/outlet at a single frequency [$f^{(E)} = 1.62$ MHz and $f^{(M)} = 1.67$ MHz]. Indeed, the FEA results suggest that similar mode shapes exist throughout the range from 1.5 MHz to 1.7 MHz with a second local maximum in tip pressure at $f^{(M)} = 1.52$ MHz (Fig. 9f). Because the CR cells dynamically redistribute within the changing acoustic field, they enable detection of two nearly overlapping resonances. Distinct peaks in image correlation coefficient discriminate between the third ejection mode [$f^{(E)} = 1.60$ MHz] and the second half-wavelength resonance [$f^{(E)} = 1.66$ MHz] of the left/right domain (see potential line plots in Fig. 9c). Although the passive beads resemble the desired field structure within the central chamber, the undulating terminal distribution is likely due to the influence of a coincident lateral resonance. The CR cell distribution density confirms this observation with tighter aggregation at certain locations along the lateral ($x$-) direction for both the central chamber and left/right domain resonances; however, the ejection mode identified by the CR cells has superior longitudinal stratification to that identified by the PS beads. Finally, the CR cells capture real-world irregularities with some experimental repeats showing an asymmetric field distribution due to slight differences in device assembly (note bands depicting standard deviation in Fig. 9a).

## Conclusions

Inadequate metrology is a critical barrier to wider adoption of acoustic microfluidic devices in clinical and industrial settings. The use of active, living probes for dynamic measurements and/or device calibration could be an enabling technology in

this context. Randomly swimming cells, a form of active matter, can visually display fluctuations in system performance due to changing operating conditions or environmental variables in real-time, which is not feasible using extant experimental methods. This capability provides a potential experimental alternative to model-based design and optimization, enabling exploration of device performance with a level of detail previously only possible using sophisticated FEA, but without the limiting assumptions of such theoretical tools.

In this work, we establish the use of *Chlamydomonas reinhardtii* (CR) cells as active probes to automatically assess acoustofluidic device resonances, including qualitative mapping of the acoustic field strength. Swimming CR cells not only identify resonant frequencies for 1D and 2D geometries, but also discriminate between resonances based on their relative strength, suggesting that this approach could be used to estimate and compare the quality factors for peaks in image correlation coefficient. The 2D circular chamber and more complex uMIST chip illustrate further advantages over FEA. Here, the visualized acoustic fields capture real-world irregularities due to imperfect device assembly or asymmetries in the inlet/outlet channels.

CR cells prove to be excellent probes of acoustofluidic performance. They exhibit uniform size distributions with an average size that is well-suited to manipulation by low-MHz frequency ultrasound. Because they are algae cells, they require no special incubator, or institutional biological and chemical (IBC) safety protocols as might be required for mammalian cells. As important as their physical properties, straightforward maintenance and preparation expand their accessibility to researchers unfamiliar with biological techniques. The

qualitative results presented here are compelling evidence of the practical benefits to the acoustic microfluidics community.

More precise quantification of device performance is still needed to directly compare different devices and platforms. We are currently performing detailed measurements of the acoustophysical and dynamic properties for various CR cell strains, which will allow us to connect the swimming cell distribution density to the local acoustic energy density throughout any arbitrary microfluidic domain. By advancing CR cells as practical probes for performance measurement, we hope to accelerate translation of research prototypes to commercial products and to improve the long-term viability of acoustofluidic devices.

## Conflicts of interest

There are no conflicts to declare.

## Acknowledgements

## References

1. A. Huang, M. Miansari and J. Friend, *Appl. Phys. Lett.*, 2018, **113**, 034103.
2. M. M. Binkley, M. Cui, W. Li, S. Tan, M. Y. Berezin and J. M. Meacham, *Phys. Fluids*, 2019, **31**, 082007.
3. P. H. Huang, S. G. Zhao, H. Bachman, N. Nama, Z. S. Li, C. Y. Chen, S. J. Yang, M. X. Wu, S. P. Zhang and T. J. Huang, *Adv. Sci.*, 2019, **6**, 1900913.
4. M. M. Binkley, M. Y. Cui, M. Y. Berezin and J. M. Meacham, *ACS Biomater. Sci. Eng.*, 2020, **6**, 6108-6116.
5. J. M. Meacham, A. O'Rourke, Y. Yang, A. G. Fedorov, F. L. Degertekin and D. W. Rosen, *J. Manuf. Sci. Eng.*, 2010, **132**, 030905.
6. R. R. Collino, T. R. Ray, R. C. Fleming, J. D. Cornell, B. G. Compton and M. R. Begley, *Extreme Mech. Lett.*, 2016, **8**, 96-106.
7. D. S. Melchert, R. R. Collino, T. R. Ray, N. D. Dolinski, L. Friedrich, M. R. Begley and D. S. Gianola, *Adv. Materials Technol.*, **4**, 1900586.
8. M. J. Varady, L. McLeod, J. M. Meacham, F. L. Degertekin and A. G. Fedorov, *J. Micromech. Microeng.*, 2007, **17**, S257-S264.
9. A. G. Fedorov and J. M. Meacham, *IEEE Trans. Compon. Packag. Technol.*, 2009, **32**, 746-753.
10. A. Huang, H. D. Liu, O. Manor, P. Liu and J. Friend, *Adv. Mat.*, 2020, **32**, 1907516.
11. J. Hultstrom, O. Manneberg, K. Dopf, H. M. Hertz, H. Brismar and M. Wiklund, *Ultrasound Med. Biol.*, 2007, **33**, 145-151.
12. J. J. Shi, D. Ahmed, X. Mao, S. C. S. Lin, A. Lawit and T. J. Huang, *Lab Chip*, 2009, **9**, 2890-2895.
13. B. Vanherberghen, O. Manneberg, A. Christakou, T. Frisk, M. Ohlin, H. M. Hertz, B. Onfelt and M. Wiklund, *Lab Chip*, 2010, **10**, 2727-2732.
14. M. Wiklund, *Lab Chip*, 2012, **12**, 2018-2028.
15. M. A. Burguillos, C. Magnusson, M. Nordin, A. Lenshof, P. Augustsson, M. J. Hansson, E. Elmer, H. Lilja, P. Brundin, T. Laurell and T. Deierborg, *PLoS One*, 2013, **8**, e64233.
16. A. Ku, H. C. Lim, M. Evander, H. Lilja, T. Laurell, S. Scheding and Y. Ceder, *Anal. Chem.*, 2018, **90**, 8011-8019.
17. M. X. Wu, Y. S. Ouyang, Z. Y. Wang, R. Zhang, P. H. Huang, C. Y. Chen, H. Li, P. Li, D. Quinn, M. Dao, S. Suresh, Y. Sadovsky and T. J. Huang, *Proc. Natl. Acad. Sci. U. S. A.*, 2017, **114**, 10584-10589.
18. M. X. Wu, C. Y. Chen, Z. Y. Wang, H. Bachman, Y. S. Ouyang, P. H. Huang, Y. Sadovsky and T. J. Huang, *Lab Chip*, 2019, **19**, 1174-1182.
19. D. Carugo, T. Octon, W. Messaoudi, A. L. Fisher, M. Carboni, N. R. Harris, M. Hill and P. Glynne-Jones, *Lab Chip*, 2014, **14**, 3830-3842.
20. P. Ohlsson, M. Evander, K. Petersson, L. Mellhammar, A. Lehmusvuori, U. Karhunen, M. Soikkeli, T. Seppa, E. Tuunainen, A. Spangar, P. von Lode, K. Rantakokko-Jalava, G. Otto, S. Scheding, T. Soukka, S. Wittfooth and T. Laurell, *Anal. Chem.*, 2016, **88**, 9403-9411.
21. P. Li, Z. M. Mao, Z. L. Peng, L. L. Zhou, Y. C. Chen, P. H. Huang, C. I. Truica, J. J. Drabick, W. S. El-Deiry, M. Dao, S. Suresh and T. J. Huang, *Proc. Natl. Acad. Sci. U. S. A.*, 2015, **112**, 4970-4975.
22. M. Antfolk, C. Magnusson, P. Augustsson, H. Lija and T. Laurell, *Anal. Chem.*, 2015, **87**, 9322-9328.
23. X. J. Hu, S. K. Zhao, Z. Y. Luo, Y. F. Zuo, F. Wang, J. M. Zhu, L. F. Chen, D. Y. Yang, Y. J. Zheng, Y. X. Cheng, F. L. Zhou and Y. Yang, *Lab Chip*, 2020, **20**, 2228-2236.
24. X. J. Hu, J. M. Zhu, Y. F. Zuo, D. Y. Yang, J. J. Zhang, Y. X. Cheng and Y. Yang, *Lab Chip*, 2020, **20**, 3515-3523.
25. M. Kim, E. Huff, M. Bottier, S. K. Dutcher, P. V. Bayly and J. M. Meacham, *Soft Matter*, 2019, **15**, 4266-4275.
26. J. X. Zhang, S. J. Yang, C. Y. Chen, J. H. Hartman, P. H. Huang, L. Wang, Z. H. Tian, P. R. Zhang, D. Faulkenberry, J. N. Meyer and O. J. Huang, *Lab Chip*, 2019, **19**, 984-992.
27. A. D. Ledbetter, H. N. Shekhani, M. M. Binkley and J. M. Meacham, *IEEE Trans. Ultrason. Ferroelectr. Freq. Control*, 2018, **65**, 1893-1904.
28. P. Hahn, I. Leibacher, T. Baasch and J. Dual, *Lab Chip*, 2015, **15**, 4302-4313.
29. F. Garofalo, T. Laurell and H. Bruus, *Phys. Rev. Appl.*, 2017, **7**, 054026.
30. R. Barnkob, P. Augustsson, T. Laurell and H. Bruus, *Lab Chip*, 2010, **10**, 563-570.
31. T. Cacace, V. Bianco, M. Paturzo, P. Memmolo, M. Vassalli, M. Fraldi, G. Mensitieri and P. Ferraro, *Lab Chip*, 2018, **18**, 1921-1927.
32. P. Augustsson, R. Barnkob, S. T. Wereley, H. Bruus and T. Laurell, *Lab Chip*, 2011, **11**, 4152-4164.
33. R. Barnkob, P. Augustsson, T. Laurell and H. Bruus, *Phys. Rev. E*, 2012, **86**, 056307.
34. R. Barnkob, I. Iranmanesh, M. Wiklund and H. Bruus, *Lab Chip*, 2012, **12**, 2337-2344.
35. G. Thalhammer, R. Steiger, M. Meinschad, M. Hill, S. Bernet and M. Ritsch-Marte, *Biomed. Opt. Express*, 2011, **2**, 2859-2870.

ARTICLE

36. P. G. Bassindale, D. B. Phillips, A. C. Barnes and B. W. Drinkwater, *Appl. Phys. Lett.*, 2014, **104**, 163504

37. A. Lamprecht, S. Lakamper, T. Baasch, I. A. T. Schaap and J. Dual, *Lab Chip*, 2016, **16**, 2682-2693.

38. J. van't Oever, R. Frentrop, D. Wijnperle, H. Offerhaus, D. van den Ende, J. Herek and F. Mugele, *Appl. Opt.*, 2015, **54**, 6482-6490.

39. V. Vitali, G. Core, F. Garofalo, T. Laurell and A. Lenshof, *Sci. Rep.*, 2019, **9**, 19081

40. W. Yan and J. F. Brady, *Soft Matter*, 2015, **11**, 6235-6244.

41. S. C. Takatori, R. De Dier, J. Vermant and J. F. Brady, *Nat. Comm.*, 2016, **7**, 1-7

42. L. P. Gorkov, *Dokl. Akad. Nauk SSSR*, 1961, **140**, 88-91.

43. M. Barmatz and P. Collas, *J. Acoust. Soc. Am.*, 1985, **77**, 928-945.

44. Z. Shaglwf, B. Hammarstrom, D. S. Laila, M. Hill and P. Glynne-Jones, *J. Acoust. Soc. Am.*, 2019, **145**, 945-955.

45. G. T. Silva and H. Bruus, *Phys. Rev. E*, 2014, **90**, 063007.

46. S. Sepehrirahnama, K. M. Lim and F. S. Chau, *J. Acoust. Soc. Am.*, 2015, **137**, 2614-2622.

47. S. Z. Hoque and A. K. Sen, *Phys. Fluids*, 2020, **32**, 072004.

48. S. M. Hagsater, T. G. Jensen, H. Bruus and J. P. Kutter, *Lab Chip*, 2007, **7**, 1336-1344.

49. J. M. Meacham, M. J. Varady, F. L. Degertekin and A. G. Fedorov, *Phy. Fluids*, 2005, **17**, 100605

50. J. A. Holmes and S. K. Dutcher, *J. Cell Sci.*, 1989, **94**, 273-285.

51. B. Xie, S. Bishop, D. Stessman, D. Wright, M. H. Spalding and L. J. Halverson, *ISME J.*, 2013, **7**, 1544-1555.

52. G. V. Rossum and F. L. Drake, PYTHON 2.6 Reference Manual, 2009.

53. MATLAB r2017b, The MathWorks Inc., 2017.

54. F. Crameri, 2018, DOI: 10.5281/zenodo.1243862, code repository at www.fabiocrameri.ch/colourmaps

55. J. S. Guasto, K. A. Johnson and J. P. Gollub, *Phys. Rev. Lett.*, 2010, **105**, 168102.

56. B. Qin, A. Gopinath, J. Yang, J. P. Gollub and P. E. Arratia, *Sci. Rep.*, 2015, **5**, 9190.

57. J. M. Meacham, C. Ejimofor, S. Kumar, F. L. Degertekin and A. G. Fedorov, *Rev. Sci. Instrum.*, 2004, **75**, 1347-1352.